Effective contact texture region aware pavement skid resistance prediction via convolutional neural network

Shi, Weibo; Niu, Dongyu; Li, Zirui; Niu, Yanhui

DOI
10.1111/mice.13063

Publication date
2023

Document Version
Final published version

Published in
Computer-Aided Civil and Infrastructure Engineering

Citation (APA)
Shi, W., Niu, D., Li, Z., & Niu, Y. (2023). Effective contact texture region aware pavement skid resistance prediction via convolutional neural network. *Computer-Aided Civil and Infrastructure Engineering*. https://doi.org/10.1111/mice.13063

DOI: 10.1111/mice.13063

INDUSTRIAL APPLICATION

COMPUTER-AIDED CIVIL AND INFRASTRUCTURE ENGINEERING WILEY

Effective contact texture region aware pavement skid resistance prediction via convolutional neural network

Weibo Shi[1,2] | **Dongyu Niu**[1,2] | **Zirui Li**[3,4] | **Yanhui Niu**[1,2]

[1]School of Materials Science and Engineering, Chang'an University, Xi'an, China

[2]Engineering Research Center of Transportation Materials of the Ministry of Education, Chang'an University, Xi'an, China

[3]School of Mechanical Engineering, Beijing Institute of Technology, Beijing, China

[4]Department of Transport and Planning, Faculty of Civil Engineering and Geosciences, Delft University of Technology, Delft, The Netherlands

Correspondence
Dongyu Niu, School of Materials Science and Engineering, Chang'an University, Xi'an 710061, China.
Email: niudongyu_1984@chd.edu.cn

Funding information
The Natural Science Foundation of China, Grant/Award Number: No. 51608045; Shaanxi Housing and Urban-Rural Development Science and Technology Project, Grant/Award Number: 2020-K11; The Special Fund for Basic Scientific Research of Central Colleges, Grant/Award Number: No. 300102310301

Abstract

The surface texture of asphalt pavement has a significant effect on skid resistance performance. However, its contribution to the performance of skid resistance is non-homogeneous and subjects to local validity. There are also a few deep learning models that take into account the effective contact texture region. This paper proposes a convolutional neural network model based on the effective contact texture region, containing macro- and micro-scale awareness sub-modules. In this study, the asphalt mixture with varying gradations was designed to accurately obtain the effective contact texture region. Then, the textures were disentangled into macro- and micro-texture scales by applying the fast Fourier transform and fed into the model for training. Finally, the area of effective contact texture region was calculated, and the effective contact ratio parameter was then proposed using the triangulation algorithm. The results showed that the effective contact texture area of pavement varies by the asphalt mixture type. The effective contact ratio parameter exhibited a significant positive correlation (*Pearson correlation coefficient* is 0.901, $R^2 = 0.8129$) with skid resistance performance and was also influenced by key sieve aggregate content from 2.36 to 4.75 mm. The data of effective contact texture region following disentanglement significantly released the model performance (the relative error dropped to 1.81%). The model exhibited improved precision and performance, which can be utilized as an efficient, non-contact alternative method for skid resistance analysis.

1 | INTRODUCTION

The skid resistance of a road surface is a crucial part of the performance component since it largely impacts the driving safety of a vehicle. For road surfaces, skid resistance refers to the ability of the road surface to resist wheel slip. This essential property is mainly composed of the horizontal cutting force provided by the aggregates in the asphalt mixture and the adhesive force of the asphalt binder. According to studies, numerous traffic accidents are directly attributable to the absence of skid resistance on the roadway (WHO, 2018). Under adverse conditions such as rain, the contact area between the road surface and the wheels is significantly reduced. The decrease in skid resistance contributes to an increase in traffic accidents and fatalities, particularly during snow and ice. However, when the skid resistance of the road surface is increased by more than 10%, the likelihood of traffic accidents decreases by approximately 13% (Ahammed & Tighe, 2009). Thereby, enhancing the surface skid resistance of the pavement under various difficult conditions and improving the interaction between the pavement and the tire is a promising direction.

Appropriate research methods are essential for the in-depth investigation of the skid resistance mechanism. The earlier research on the skid resistance of road surface has focused on the development of skid resistance testing equipment and the improvement of testing methodologies. Still, most of them are direct friction tests (Kumar et al., 2021), such as the pendulum tester (Kulakowski et al., 1990), dynamic friction testing (L. Chu et al., 2019), Grip-Tester (Kouchaki et al., 2018), and so on. Among these, the pendulum tester has been proven to be the most accurate in terms of friction mechanism in actual situations (L. J. Chu & Fwa, 2019).

Although such methods (ASTM E303-93, 2018, JTG 3450-2019, 2019) and equipment (Han et al., 2018; Wasilewska et al., 2020) are continually being improved, the conventional direct testing method will always be time-consuming and inefficient concerning the traffic opening. The non-contact testing and pavement texture analysis techniques based on digital images are becoming increasingly indispensable tools for skid resistance studies due to the portability of the sampling equipment (Puzzo et al., 2017; Vilaca et al., 2010) and the efficacy of the analysis (Wesolowski et al., 2018; Yan et al., 2020).

Given various advantages of non-contact measurement methods, many studies have demonstrated the link between pavement texture and pavement skid resistance (Dong et al., 2022; Han et al., 2019; Kogbara et al., 2016). Yan et al. (2020) adopted a laser scanner to obtain point clouds data. They characterize pavement texture features with texture spectra using selected in-service pavements. After determining the relationship between spectral analysis and field measurement results, they observed a positive correlation between pavement texture spectra and friction coefficients. Further investigations by Celko et al. (2016) and Wang et al. (2018) exhibited that the two-dimensional texture feature parameters do not contain richer texture information. In addition, studies by Hofko et al. (2019) and Zhang et al. (2019) demonstrated a significant correlation between the reduction of pavement texture profile and the deterioration of skid resistance. The existing studies on the skid resistance of non-contact pavements can be divided into two main categories: statistical texture feature parameter analysis and frequency and signal-based macro–micro texture analysis. Overall, the relationship between pavement texture and pavement skid resistance is evident.

Considering the validity of the contact between the textured region of the road surface and the vehicle tire, the texture is not in complete contact with the tread. Thus, Kogbara et al. (2018) found that the peak density and peak volume at the top of the region down to a depth of 2 mm contribute significantly to the skid resistance, with the density effect being more significant than the volume effect. Ding et al. (2021) obtained the relationship between friction values and surface area of textured regions at different depths by using digital image processing techniques. The results indicated that the skid resistance of the pavement is significantly and positively correlated with the surface area of textured areas in the range of 0.5 to 2 mm in depth. Yang, Wang et al. (2021) used discrete wavelet transforms to decompose 3D pavement data into 11 texture types with different wavelengths and adopted cross-validation and stepwise multiple linear regression to analyze them. They reported that the pavement textures with wavelengths not exceeding 3.2 mm in the maximum 2.5 mm depth range of the pavement can be used as an effective tire–pavement contact area. Most of the above-mentioned studies investigated the distribution characteristics of pavement texture in a comparatively informative way. All evidence suggests that the effective area of surface pavement texture exists objectively. It is necessary to formally consider the effective region of pavement texture in skid resistance studies.

Due to the outstanding nonlinear expression capability, data abstraction, and analysis, machine learning methods and neural network models are increasingly used (Adeli, 2001, 2020) in civil engineering. With the development of supervised and unsupervised learning, efficient and robust paradigms (Alam et al., 2020; Rafiei et al., 2017) are gradually derived, which has greatly improved the efficiency and accuracy of work in areas such as road crack identification (Chen & He, 2022; C. Liu et al., 2022; Żarski et al., 2022) and road condition evaluation (Grande et al., 2017; Jeong et al., 2020).

Especially in the field of road skid resistance studies, the combination of macroscopic (Najafi et al., 2016; Qiang Joshua Li, 2017) and microscopic texture statistics parameters (Yang et al., 2021; Zhan et al., 2022) with machine learning or deep learning has driven skid resistance studies into the new era. Nevertheless, such models commonly require a manual selection of feature indicators followed by supervised learning. Their accuracy and generalization ability are usually affected by the degree of accuracy of feature engineering. Aiming for generalized metrics is not easy to achieve. In response to these uncertainties, it is necessary to adopt a better paradigm.

The convolutional neural network (CNN) model is particularly well-suited for feature extraction and fitting pavement non-contact test data as a classical algorithm of deep learning with the assistance of high perception and abstraction capacity of spatial features using convolutional intercorrelation algorithm. Yang et al. (2018) used an onboard texture scanner to obtain a 3D point cloud for a certain length of a route and calculated mean depth (MPD) per unit of a route length as an evaluation index and transformed the scanned pavement section lines into a spectral map as the input of a CNN model to rate the skid resistance of the pavement. Zhan et al. (2020) summarized the previous studies, extended the acquisition source of pavement area texture data while using the grip test results as an index, and validated the high accuracy and performance of the model based on the residual CNN, that is, ResNet. Tong et al. (2018) utilized a handheld scanner to acquire the regional surface texture of pavement core specimens, transformed it into a pixel-like two-dimensional matrix, then provided as an input into a CNN model to estimate the level of pavement skid resistance with MPD value. Lu et al. (2022) developed a CNN model to investigate the primary relationship between the texture and the field-level skid-resistance measurement of the pavement. They investigated the relationship between the texture acquisition interval and the effective contact. It was concluded that textures with wavelengths higher than 2.4 mm were critical for wet friction. The effective texture contact area is 0.6 times the original region, verifying the capacity of the model to maintain relative error at 14%. The utilization of CNNs in the study of pavement skid resistance has achieved tremendous success. However, the majority of studies have not paid enough attention to the effectiveness of the texture region contributing to antiskid performance. There is still much potential for improvement in studies that coupled CNN models with studies of skid resistance.

The tire–road interaction is complicated during the actual vehicle driving process. There is a maximum depth limit for the natural contact area (B. Chen et al., 2017; Ding et al., 2021). This indicates that the contribution of the texture configuration to the skid resistance of the pavement is insufficient and uneven, and there is discrepancy in the texture distribution in different areas. However, most of the prior models do not adequately account for the effective contact region between the pavement surface and the rubber tire. Presently, few studies match the skid resistance test area with the texture acquisition area, which leads to supervised model training metrics that do not necessarily meet reality. The relationship between the features learned by the model and the actual measured labels would not correspond precisely to each other.

The existing studies on pavement skid resistance using CNN models tend to achieve favorable outcomes, which are closely related to the preparation of large datasets, model architecture preferences, and training methods. Still, there is a dynamic balance between performance and overhead of neural networks (Bengio & Lecun, 2007; Pascanu et al., 2013). Well-designed structures and sample expansion can reduce unnecessary resource consumption (Zhuang Liu et al., 2022). It is time-consuming and expensive to train complex models if large-volume datasets are prepared for indoor experiments. Conversely, the models are not easy to achieve good fitting accuracy, which is the difficulty of building models using indoor experiments. The existing CNN-based pavement skid resistance research results are relatively scattered and cannot be quickly generalized for application. Therefore, it is required to develop a CNN model with concise logic, high accuracy, and fast generalization for various types of pavements.

Given this, the paper proposes a CNN model based on the effective contact texture region. The region of the captured texture is tested for skid resistance using a British pendulum tester (BPT). Disentanglement of effective textures was performed by frequency analysis at macro- and micro-scales. A mapping paradigm between the effective contact texture region to the skid resistance of the pavement is established to predict the skid resistance of pavement. Finally, the area of the effective contact texture region is calculated by triangulation. Its distribution characteristics and influencing factors have been studied thoroughly. It provides new insights into asphalt pavement skid resistance research and material design.

2 | METHODOLOGY

2.1 | Framework

In this paper, in order to study the role of effective texture contact effect on the skid resistance of asphalt pavement, tests are conducted on asphalt mixture rutting slabs that are prepared by indoor experiments, At the same time, collection and processing methods of scanning area samples are improved, and the technical route of this study is illustrated in Figure 1.

2.2 | Specimen preparation

In this study, asphalt pavement is used as the research object, and tests are conducted in the laboratory by forming asphalt mixture rutting plate specimens. The performance of the base asphalt (Table 1) used to make the asphalt mixture is tested according to the Chinese specification JTG E20-2019 (JTG E20-2019, 2019).

Based on the AC-13 asphalt mixture (JTG F40-2004, 2005), a total of nine types of varying gradations are designed by controlling the different key sieve passing rates (Table 2), and the gradation curves are shown in Figure 2. All aggregates are obtained from locally produced limestone in Shaanxi Province, China.

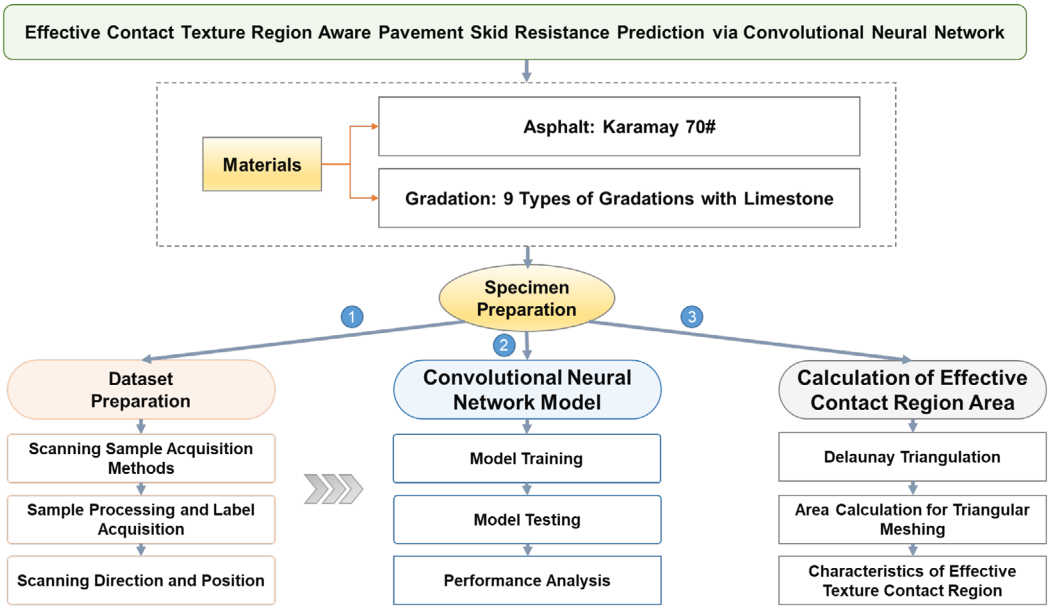

FIGURE 1 Framework for the study.

TABLE 1 Asphalt performance parameters.

Type of asphalt	Performance parameters		Indicators
Karamay 70#	Penetration (25°C, 5 s, 100 g)/0.1 mm		66
	Ductility (15°C, 5 cm/min)/cm		>100
	Softening point/°C		50.5
	RTFOT	Quality loss/%	−0.512
		Penetration ratio/%	71
		Residual ductility (15°C, 5 cm/min)/cm	20

Note: RTFOT means Rolling Thin Film Oven Test.

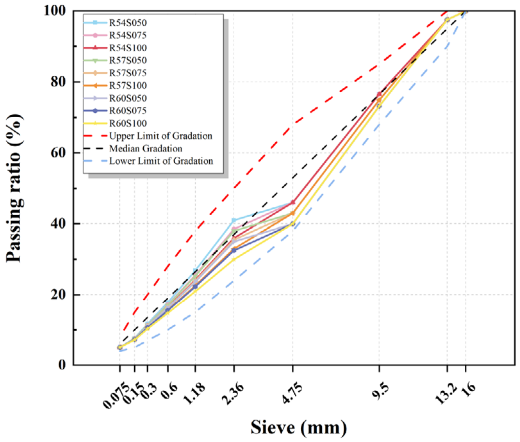

FIGURE 2 Asphalt mixture gradation curve for this experiment.

2.3 | Dataset preparation

2.3.1 | Scanning sample acquisition methods

The preparation of the dataset is a critical step in the subsequent CNN model training. Its accuracy and precision almost determine the correctness of the whole model. In this study, a 3D laser texture scanner (LTS), model LTS-9400HD, manufactured by AMES, is utilized to obtain the texture point clouds. This Workstation-type scanner is little affected by the difference in surface gloss and abrupt changes in the elevation of the sample. Its scanning accuracy is higher than the handheld laser scanner, and the main technical parameters of the scanner are shown in Table 3.

According to the specification (ISO 13473-1, 2020), the sampling spacing should not exceed 1 mm for texture analysis, while the specification (ASTM E1845, 2015) specifies that the sampling resolution in the vertical direction

TABLE 2 Gradation and optimum asphalt content.

Gradation	Passing rate/%										OAC/%
	16	13.2	9.5	4.75	2.36	1.18	0.6	0.3	0.15	0.075	
R54S050	100.0	97.5	76.6	46.0	41.0	26.9	17.8	11.6	7.6	5.0	4.76
R54S075	100.0	97.5	76.6	46.0	38.5	25.5	17.1	11.4	7.5	5.0	4.60
R54S100	100.0	97.5	76.6	46.0	36.0	24.2	16.4	11.1	7.4	5.0	4.44
R57S050	100.0	97.5	74.9	43.0	38.0	25.3	17.0	11.3	7.5	5.0	4.67
R57S075	100.0	97.5	74.9	43.0	35.5	23.9	16.3	11.0	7.4	5.0	4.55
R57S100	100.0	97.5	74.9	43.0	33.0	22.6	15.6	10.7	7.3	5.0	4.42
R60S050	100.0	97.5	73.2	40.0	35.0	23.7	16.2	10.9	7.4	5.0	4.58
R60S075	100.0	97.5	73.2	40.0	32.5	22.3	15.5	10.6	7.3	5.0	4.48
R60S100	100.0	97.5	73.2	40.0	30.0	20.9	14.7	10.3	7.2	5.0	4.38

Note: R54 in R54S050 means 54% of the aggregate above 4.75 mm, while S050 means 5% of the aggregate between 2.36 and 4.75 mm. OAC means optimum asphalt content.

TABLE 3 Key technical parameters of the scanner.

Parameters	Value
Maximum resolution in the length direction (mm)	0.00635
Maximum resolution in the width direction (mm)	0.02469
Vertical Resolution (mm)	0.005
Scanning speed (line/s)	4.5

should be less than 0.05 mm. The sampling spacing should be no more than 1.00 mm.

If the maximum resolution is adopted to scan the data in this study, the average single region takes up to 3.65 h. Moreover, the sampling accuracy (Ding et al., 2021; Lu et al., 2022) has an impact on the performance of the neural network model. Thus, this study searches for a balance between high accuracy and efficient acquisition under the premise of satisfying the specification and chooses the scan length and width direction resolutions of 0.0740 and 0.0254 mm, respectively, which can reduce the single sampling elapsed time about to 1 h.

2.3.2 | Scanning direction and position

Based on the definition of pavement skid resistance and specification standards, skid resistance analysis using pavement surface texture requires that samples are to be collected from the longitudinal section of the pavement in the direction of the axis. The sampling direction on the specimens in this study was the same as the rolling direction in which the rutted slab specimens were made, while the field sampling was aligned with the direction of the carriageway.

Considering the distinctive contributions of texture distribution to the skid resistance of the pavement, the length of the scanning area in this study is set to the sliding distance necessary for the pendulum tester, that is, 126 mm. The width of the scanning area is set to be slightly wider than two times the width of the pendulum slider, that is, 51 mm. The necessary extra space is left here for the transition to a steady-state resolution of the scanner laser. But the real size of the entire sampling area is unified in the formal data processing phase as 126 mm × 25.4 mm × 2.

To ensure the consistent location of the sampling and testing areas, an area positioning gauge is made of acrylic plastic, which has the same outer dimensions as the rutting plate specimen. The internal sizes are set according to the above principles. Each partition number is $i \in \{1,2,3,4,5,6\}$. The samples are obtained by the single-area dual sampling method, with a total of 12 pieces in six partitions for each specimen, and the specific collection locations are shown in Figure 3.

2.3.3 | Sample preparation and label acquisition

Sample Preprocessing

Although high-performance, low-sensitivity scanners can minimize the impact of such shortcomings, they cannot eliminate noise or bad spots. The bad point is an extreme form of noise, usually manifested as a point where the elevation rate of variation tends to infinity. In this study, they are collectively referred to as noise.

In addition, the scanned data usually have problems such as skewed or tilted sections due to uneven placement of the specimen or uneven surface to be measured. Therefore, calibration is also required for the collected raw samples.

The noise collected by the device (the field of view shows the burr or spike area) is often detected by the quadrature point method, substituted by the minimum value of the neighborhood. This method replaces the noisy points on the scan line with the minimum value of the elevation of

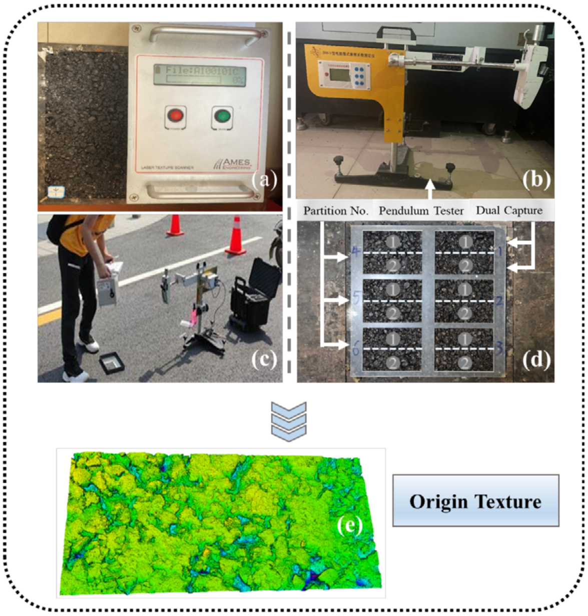

FIGURE 3 Data acquisition example: (a) the laser scanner and specimen sampling, (b) the pendulum tester, (c) field sampling, (d) sampling rules, and (e) original point cloud.

the neighboring points before and after it as illustrated in Equations (1) and (2).

$$S_n = \{z_n > 1.5Q_u or z_n < 1.5Q_l\} \tag{1}$$

$$Z'n = \min(z_{n-1}, z_{n+1}) \tag{2}$$

where S_n is the set of lousy point, and$Z'n$ is the elevation at the lousy point after the substitution; z_n is the elevation at the lousy point; z_{n-1} is the elevation of the point before the lousy point; z_{n+1} is the elevation of the point after the lousy point; n is the index of the location of the lousy point, and Q_u, Q_l are the upper and lower quartiles, respectively.

To solve the problem that the section line is skewed or biased due to uneven surface and irregular spatial position of the specimen, which leads to the deviation of the acquired point data from the accurate position information. Usually, a section elevation correction algorithm based on the principle of least squares is implemented. This method takes the scanned section as the object and uses the original skewed elevation value minus the horizontal correction distance obtained to correct the skewed elevation as shown in Equation (3).

$$Z^{(i)} = z^{(i)} - b_1 - b_0\,(i = 0, \ldots, N-1) \tag{3}$$

where $z^{(i)}$ is the pre-calibration elevation value; $Z^{(i)}$ is the corrected elevation value; i is the index of data points in the section construction line; N is the number of points collected for this construction line; b_0 and b_1 are the correction parameters for the degree of skew and offset, whereby b_1 and b_0 are calculated by Equations (4) and (5), respectively.

$$b_1 = \frac{12\sum_{i=0}^{i=N-1} iz_i - 6(N-1)\sum_{i=0}^{i=N-1} z_i}{(N-1)N(N+1)} \tag{4}$$

$$b_0 = \frac{1}{N}\sum_{i=0}^{N-1} z_i - b \times \frac{N-1}{2} \tag{5}$$

Effective contact texture region extraction

Considering the transient and partial tire–road contact, it is not easy to obtain accurate depth values of the effective contact texture region due to tire size and tread pattern, contact surface pressure, and others. Nevertheless, many studies have found that effective contact occurred within 0.5 to 2 mm (Ding et al., 2021; Kogbara et al., 2018; Yang et al., 2021).

Given this, the paper adopts the method of filtering from the top to the bottom of the texture. The maximum depth of the surface texture is taken as the threshold value of 2 mm. And the points whose depth did not exceed the maximum depth of the texture were filtered out from the 3D point matrix, and then the depth of those points that failed to meet the filtering conditions was assigned to 0. After that, the original coordinate system is reset, and the plane with the depth value of 0 is utilized as the (x, y) plane of the point array position indexxoy, while the depth (i.e., the elevation) is z-axis as shown in Figure 4a,b,d.

Finally, a total of 3000 sample regions acquired in the experimental phase are batch processed. Among them, 2700 of these samples were from the test specimens mentioned before, and 300 were from the test road. Afterward, the individual sample data files are then re-indexed as the dataset training values, and the above processes are implemented by Python.

Sample label acquisition

The label of a sample refers to the data used to represent the actual meaning of the sample in the learning algorithm. In this paper, the sample label for each effective contact texture region is the British pendulum number (BPN) value obtained by the BPT under that region. Then, the effective contact texture region and BPN mapping relationship are constructed to build the dataset required for the model, and Figure 4e shows an example of a data sample.

Texture disentanglement

The relative contribution of macro-texture and micro-texture to skid resistance is not identical under different velocity conditions. The skid resistance evaluation technique adopted in this study was the BPT test,

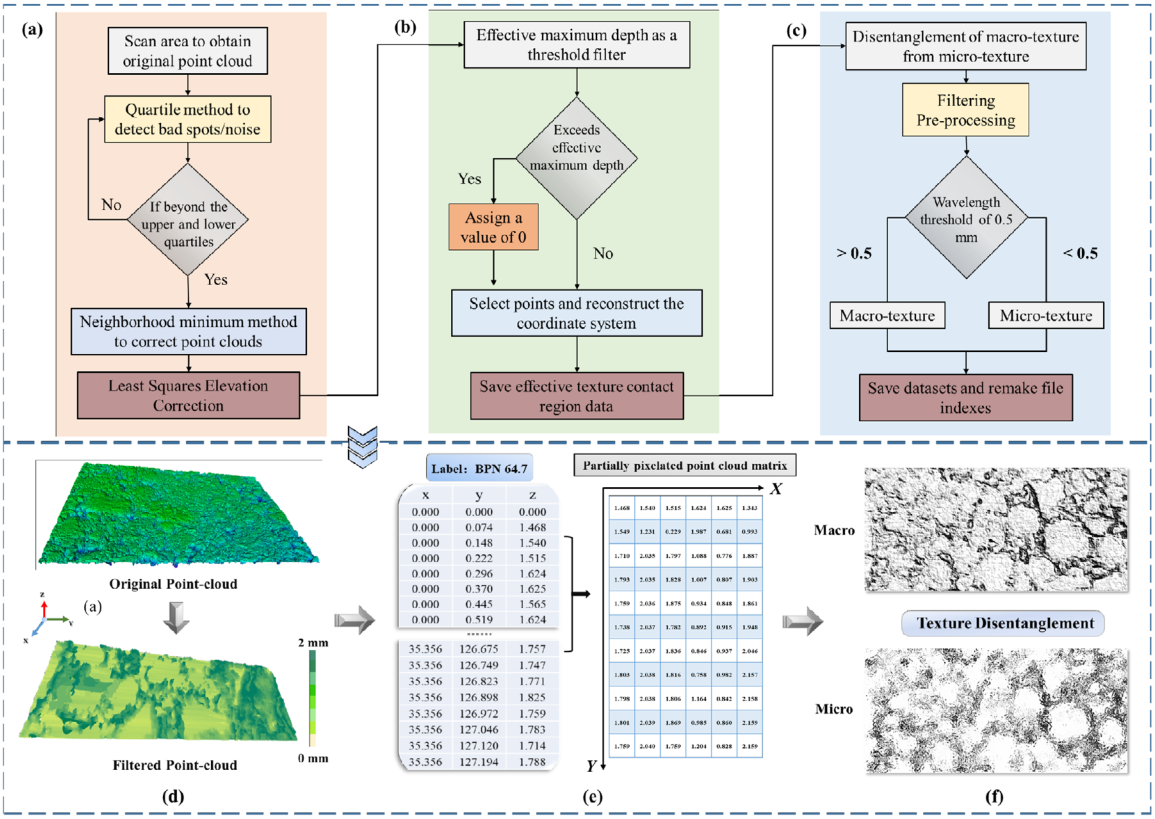

FIGURE 4 Dataset preparation: (a) Texture data preprocessing, (b) method for extraction of effective contact texture regions, (c) method for disentanglement of macro- and micro-textures, (d) example of effective depth interception, (e) original (x, y, z) elevation data and a local example of point cloud elevation matrix, and (f) an example of macro- and micro-textures in one region. BPN, British pendulum number.

which is generally known as a low-speed test. Therefore, the textures were disentangled by means of filtering whereby the neural network can focus more on identifying the features of the textures on various scales.

Initially, the frequency information of the texture is obtained by the fast Fourier transform (FFT). The texture elevation scanning lines are then filtered using an appropriate high-pass filter. The spatial frequencies below 10 m^{-1} (i.e., the wavelengths larger than 100 mm) are filtered to preserve the texture characteristics. Subsequently, a low-pass filter (LPF) is used to eliminate texture clutter with wavelengths of less than 0.1 mm.

The spatial frequency of 2000 m^{-1} (i.e., the wavelength is 0.5 mm) is identified as the boundary between macro- and micro-textures (ISO 13473-1, 2020). The effective contact texture regions obtained based on the aforementioned processing were then disentangled into two scales: macro-texture and micro-texture, as shown in Figure 4c,f. The processes above are implemented in Python.

3 | CCN MODEL: EFFECTIVETEXTURE-NET

A CNN model generally consists of a stacked combination of input, convolutional, pooling, and output layers. The input layer is the starting step of the model, and the input has a multi-channel image data matrix; the convolutional layer is the core component (i.e., also called encoder) for extracting features, which extracts the original information layer by layer to generate higher-order features; the pooling layer is utilized to enhance the main features and reduce the sensitivity of the model to the data source; the output layer is defined according to the model task to output the predicted probability or fitted value to the samples.

This study adopts the residual leap-frog connection structure to build the neural network model. The model output is the skid resistance performance (i.e., BPN value) as awarded via the effective contact texture region on macro- and micro-texture scales. The model (i.e., EffectiveTexture-Net) architecture is shown in Figure 5.

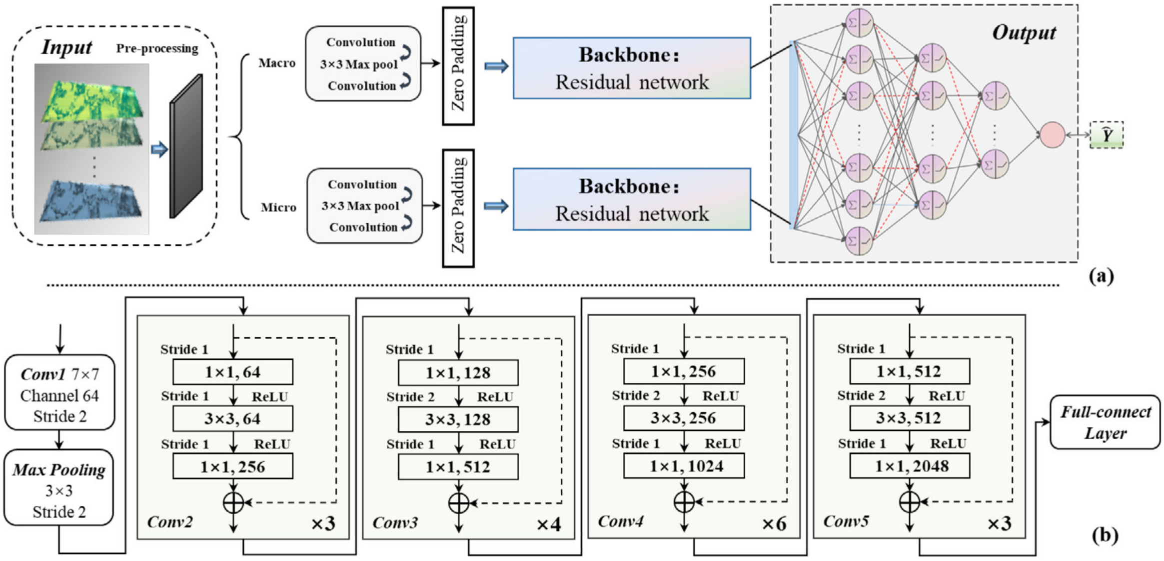

FIGURE 5 EffectiveTexture-Net model: (a) Network architecture (b) backbone of the network in detail.

3.1 | CNN model structure

This section presents the details of the CNN model utilized in the study to clearly explain the idea or logic of model construction established on the effective contact texture region.

3.1.1 | Input

The input layer, as the first layer of the model, is utilized to receive the input of the image matrix and perform preprocessing (e.g., size transformation, color gamut transformation). Then the data described in Section 2.2.3 of this paper is passed into the network backbone for feature extraction.

Inputting a raw sample into the network is essentially feeding its texture point cloud that has been disentangled at two scales (macro and micro) as shown in Figure 5a. The format of the data for each sample is downscaled from a 3D point cloud to a 2D heat map, where the rows of the matrix correspond to the position indexes of the original point matrix. The element value of each position corresponds to the value of the elevation z as shown in Figure 4e. The sample tensors will be normalized to pass into the bulk of the model.

Subsequently, the data stream initially inputs a three-layer adjustment block that consists of convolution (with kernel size of 3 × 3), max pool, convolution (with kernel size of 3 × 3), respectively, before proceeding into the corresponding sub-module for feature extraction. This serves for resizing the data tensor to be acceptable for the backbone network.

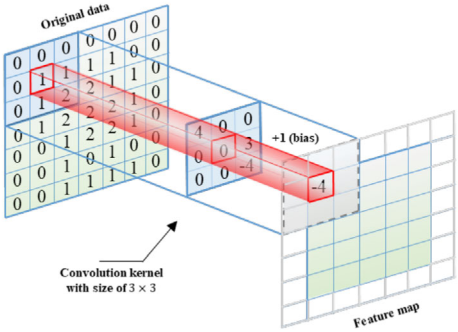

FIGURE 6 An example of a convolution operation from the dataset.

3.1.2 | Backbone of the model

The backbone of the model is the cornerstone from which the model derives features from the data. For image-like data, the convolution is an essential tool to extract the intrinsic features.

Different from the previous multi-layer perceptron model, the convolutional layer utilizes convolutional windows (also known as convolutional kernels) to implement the mutual correlation algorithm (Figure 6) to encode the data features as illustrated in Equation (6).

$$c_{ij}^{(k)} = X_{ij}^{(k)} * \omega^{(k)} + b^{(k)} \tag{6}$$

where k is the channel value; $c_{ij}^{(k)}$ is the feature encoding value at the row i and a column j in the feature map matrix; $X_{ij}^{(k)}$ is the matrix to be sampled at the row i and a column j (i.e., sampling window); $\omega^{(k)}$ is the weight matrix (i.e., convolution kernel); $b^{(k)}$denotes the deviation term,

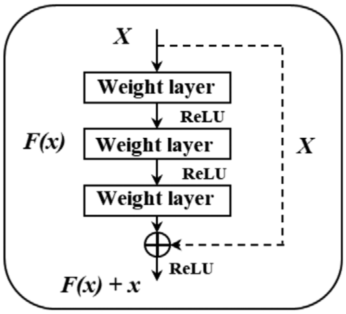

FIGURE 7 Illustration of residual structure (ReLU is the activation function).

and "*" represents the inner product operation of the matrix.

To overcome challenges such as gradient extinction and network degradation, the residual leap-frog structure has been proposed by He et al. (2016) as shown in Figure 7. This enables the neural network to deepen tremendously and to behave well at the same time.

In order to separately consider the contribution of macro-texture and micro-texture to skid resistance performance, two parallel backbone sub-modules with the same residual structure were created based on the ResNet-50. For sub-modules focusing on micro-textures, the convolution kernels were set as 1 × 1, 3 × 3, and 1 × 1 in each residual block. While for the sub-module focusing on macro-textures, the convolution kernels were set as 1 × 1, 5 × 5, and 1 × 1 in each residual block as shown in Figure 5b. The output of the two sub-modules will eventually be concatenated in dimension and then passed to the fully connected layer for regression.

The activation function is rectified linear unit (ReLU) function, that is, Equation (7). It contributes to mitigate gradient explosion or gradient disappearance during the training phase making the training terminated. The output through activation can be expressed as Equation (8).

$$F_{ReLU}\left(x\right) = \begin{cases} x, x > 0 \\ \\ 0, x \leq 0 \end{cases} \tag{7}$$

$$I^{(k)} = f_{ReLU}\left(c^{(k)}{}_{ij}\right) \tag{8}$$

where k is the channel value, $c_{ij}^{(k)}$ is the characteristic coding value at the column j of a row i in the feature map matrix, and $F_{ReLU}(x)$ is the activation function.

3.1.3 | Batch normalization

After obtaining feature maps from convolution layers, batch norm (Ioffe & Szegedy, 2015) was adopted to correct the imbalance of the data after the convolution layer and reduce the sensitivity of the algorithm to the data in the subsequent process. It contributes to accelerating model convergence, mitigating gradient dispersion, and improving model stability.

3.1.4 | Pooling layer

Pooling algorithms are typically implemented after convolution to highlight the effective information from the feature map and reduce the volume of operations.

Pooling algorithms are usually classified as average pooling and maximum pooling. The pooling window matrix manipulates the input data for the pooling operation as shown in Equation (9). The size of the data stream in the neural network model is halved, and the channels remain unchanged after pooling.

$$p_{ij}^{(k)} = pooling(X_{ij}^{(k)}) \tag{9}$$

where k is the channel value; $p_{ij}^{(k)}$ is the pooling value at the column j of a row i in the pooling matrix; $pooling(x)$ is the pooling method, and $X_{ij}^{(k)}$ is the matrix to be sampled (i.e., the pooling window) corresponding to a column j of the row i.

In this paper, the task is to identify the most salient pavement texture features and to evaluate the skid resistance accordingly. Thus, maximum pooling is chosen as the pooling layer algorithm.

3.1.5 | Fully connected layer

The fully connected layer assigns weights to the abstract features extracted by the convolutional kernel (i.e., the encoder). It maps the feature space to the sample labeling space to achieve the transformation from features to output values. The operations of each neuron in the fully connected layer can be expressed in Equation (10).

$$f_c^{(l)} = \sum_{i=0}^{n} x_i \times \omega^{(l)} + b \tag{10}$$

where n denotes the number of input neurons connected to the neuron in each layer, represents the value of each input neuron, $\omega^{(l)}$ means the weight coefficient of the neuron at the location of l in each layer, and b is the bias term.

To mitigate overfitting, this paper adopts the *Dropout* mechanism to make the layer sparse. The nodes in the fully connected layer will be randomly discarded during the learning process with a certain probability and without discrimination. This can significantly reduce the quantity of model operations and enhance the robustness of the model. This paper adopts a Dropout rate of 0.32.

3.1.6 | Output layer

Considering that the CNN model in this study aims for the effective contact texture regions for identification, the output predicts the BPN values. This is an inherent regression task rather than a classification task, so the mean square error (MSE) is chosen as the loss function.

To further mitigate the the overfitting, L2 regularization, Equation (11), is introduced in the output layer. The loss function modified by using L2 regularization, Equation (12), can reduce the weight of insignificant features and reduce the overfitting. Finally, the output layer calculates the Euclidean distance between the actual BPN value and the predicted BPN value. Then error gradient, Equation (13), will be back-propagated to the model. The fully connected layer is composed of three hidden layers with dimensions of 1024, 512, and 64. The activation function remains the same as before, also using ReLU.

$$\mathrm{L_2RT} = \frac{\lambda}{2n}\sum_{i=0}^{n}\omega_i^2 \tag{11}$$

$$f_{cost} = \frac{1}{2N}\sum_{i=1}^{N}\left(\widehat{BPN_i} - BPN_i\right)^2 + \frac{\lambda}{2n}\sum_{i=0}^{n}\omega_i^2 \tag{12}$$

$$\frac{\partial f_{\cos t}}{\partial \widehat{BPN_l}} = \frac{1}{N}\sum_{i=1}^{N}\left|\widehat{BPN_l} - BPN_i\right| \tag{13}$$

where λ is the regularization parameter; N is the number of samples; $\widehat{BPN_i}$ is the model prediction result; the BPN_i is the actual value, and $\frac{\partial f_{cost}}{\partial \widehat{BPN_i}}$ is the error gradient.

3.2 | Model training

In this paper, the forward propagation process of the CNN model to respond to the input and make predictions is similar to that of a general feedforward neural network.

In the backward propagation, to update the learnable parameters of the network, stochastic gradient descent (SGD; Ruder 2016), adaptive gradient (AdaGrad) optimization algorithm (Duchi et al., 2011), and root mean square propagation (RMSprop) optimization algorithm can usually be chosen as the training methods. However, the SGD method tends to fall into local optimum and converge slowly. The AdaGrad method tends to disappear in the middle and late stages of training and terminate the training. Compared to the former, the RMSprop optimization algorithm can alleviate the gradient disappearance caused by the rapid learning rate decrease but still needs to calculate all the gradients in the iteration process.

Therefore, the adaptive moment estimation (Adam) optimization algorithm (Kingma & Ba, 2014) is chosen as the training method in this paper, which dynamically adjusts the learning rate of each parameter using first-order moment estimation and second-order moment estimation of the gradient and ensures smooth learning of the model parameters after bias correction.

To ensure the robustness of the CNN model, the dataset was randomly partitioned each turn, where 70% of the dataset was utilized as the train set, and 30% dataset was regarded as the test set. Ten parallel isolated trials were conducted on the dataset to evaluate the model performance comprehensively.

The entire model was implemented via Pytorch (Paszke et al., 2019), while the related algorithms were implemented by using Python-based open-source libraries. The backbone parts of the model are all initialized using the weights released by Pytorch for transfer learning, and the other learnable parts are all initialized in the same way before training. The model was trained by Intel® Xeon® Platinum 8358P dual central processing unit with 512 GB RAM, and an RTX A6000 graphics processing unit with 48 GB graphic memory.

4 | AREA CALCULATION OF EFFECTIVE CONTACT TEXTURE REGION

After segmenting by the effective contact depth, there are some orphan points in the texture point clouds, which are not easy to determine the gradient at the orphan points by using the regular two-dimensional interpolation method. It is also challenging to obtain the area of the effective contact texture region by the integration method. Considering that the point cloud data obtained in this study are locally ordered and dense, the dissection is carried out based on geometric methods. A high-density triangular grid division is obtained first, after which a simple method is adopted to calculate the contact area within the effective depth region.

4.1 | Delaunay triangulation

Delaunay triangulation is a special triangulation algorithm that has two strict premises: the criterion of the empty circle and the criterion of maximizing the minimum angle. In other words, the Delaunay triangle network is unique (i.e., any four points cannot be a co-circular), where no other points exist within the outer circle of any triangle in the Delaunay triangle network. The minimum angle of the triangle formed by the Delaunay triangle profile is the

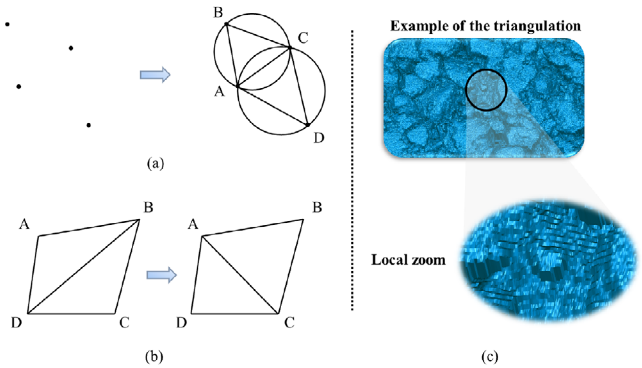

FIGURE 8 The Delaunay triangular profiling criterion: (a) empty circle guideline, (b) maximizing minimum angle criterion, and (c) an example of triangulation in a texture region.

largest among the possible triangulation of the scatter set, its geometric representation can be seen in Figure 8a,b.

4.2 | Area calculation of triangular meshes

Although Delaunay dissection is the standard for triangulation, it is algorithmically idealistic, which leads to inefficiency. Thus, this study utilizes the Bowyer–Watson algorithm (Chrisochoides & Sukup, 1999; Rebay, 1993). The method utilizes the Delaunay triangular mesh generated by point-by-point insertion. It is implemented using the Python-based *Numpy* and *Scipy* open-source libraries.

After the triangulation, the coordinates of the vertices for each triangular mesh in the space will be obtained. Then the area of this triangular mesh S_Δ can then be expressed as the absolute value of the determinant as Equation (14). The area of the entire effective contact texture region S_{ea} and the effective contact ratio $r_{contact}$ can be obtained from Equations (15) and (16). Figure 8c illustrates an example of meshing texture region by triangulation.

$$S_\Delta = \frac{1}{2}\left|\det\begin{bmatrix} 1 & 1 & 1 \\ x_1 & y_1 & z_1 \\ x_2 & y_2 & z_2 \end{bmatrix}\right| \tag{14}$$

$$S_{ea} = \sum_{i=0}^{N} S_\Delta^{(i)} \tag{15}$$

$$r_{contact} = \frac{S_{ea}}{S_{ta}} \tag{16}$$

where (x_1, y_1, z_1) and (x_2, y_2, z_2) are the coordinate representations of any two adjacent side vectors in the triangular grid; i denotes the index in the triangular grid set; N is the total number of grids, and S_{ta} is the projected area of the test area, which is also equal to the area of the rubber slider of the pendulum tester sliding.

5 | RESULTS AND DISCUSSION

So far, this study has clarified how to obtain the effective contact texture region and to build a CNN model that can be aware of the skid resistance of asphalt pavement over effective contact texture region. And then the performance of the CNN model will be evaluated whether it can be utilized as an efficient, non-contact method. Furthermore, the influencing factors of the effective contact texture region will be discussed for new perspectives on the improvement of pavement skid resistance analysis.

5.1 | Performance validation of the CNN model

5.1.1 | The performance of EffectiveTexture-Net

The model is trained with a combination of Adam optimizer, Dropout mechanism, and L2 regularization method, which can significantly improve the learning efficiency and performance in the training process. The root mean squared error (RMSE) is then used as a criterion to estimate the accuracy of the model proposed in the paper as shown in Equation (17).

$$RMSE = \sqrt{\frac{1}{N} \times \sum_{i=1}^{N} \left(\widehat{BPN}_i - BPN_i\right)^2} \tag{17}$$

where N is the number of samples; $\widehat{BPN}_i$ is the model prediction result; the BPN_i is the actual value.

The whole training process consists of 100 epochs, one of which contains 100 iterations. The training set is traversed in one iteration for a batch size of 24 samples per input. The actual average training time for one epoch is about 35 min, which is 67% and 38% less than the time taken by the SGD optimizer and the RMSprop optimizer, respectively. The training error of the model using the Adam optimizer is shown in Figure 9.

It can be seen that the difference between the prediction of model for pavement BPN values and the real measurement results is very significant after the initialization. But with the iterations increasing, the error decreases rapidly.

When the iteration reaches the 10th time, fluctuations occurred in the training. However, due to the contribution of the *Dropout* mechanism and *L2* regularization, the model gradually reaches the balance in the confrontation between underfitting and overfitting when the epoch is around the 55th time. The error variance remains stable for a more extended period, which indicates that the model

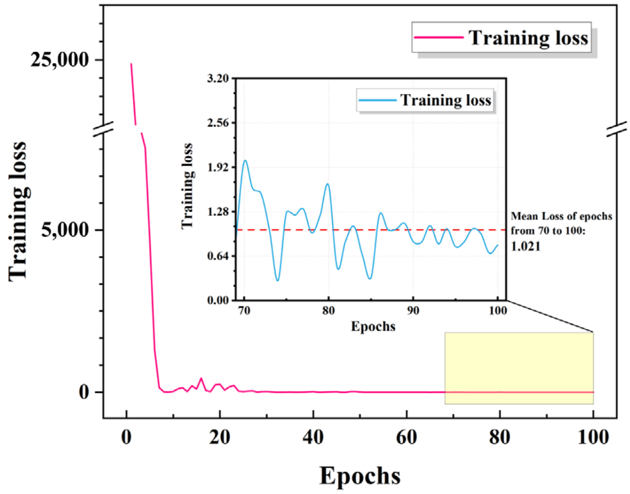

FIGURE 9 The trend of training error.

training is completed. The average absolute training error of final epochs (from 70 to 100) is 1.021.

For the performance evaluation of region skid resistance, EffectiveTexture-Net can be percept by extracting the abstract features from the effective contact texture regions. Thus, this paper utilizes the error level between the predicted BPN values and the real test BPN values to evaluate the perceptual field characterization capability of the EffectiveTexture-Net. The sample size of the total test set is 900, and the model prediction performance is shown in Figure 10.

The mean absolute error of the model on the test set was 1.232, while the mean relative error was 1.81% over 10 parallel isolated trials (mentioned in Section 3.2) of the model training.

In comparison, the percentage for the samples of predicted BPN values larger than or equal to the measured BPN values is 46.67%, with a mean absolute error of 1.264 and a mean relative error of 1.86%. While the percentage for the samples of predicted BPN values less than the measured BPN values is 53.33%, with a mean absolute error of 1.189 and a mean relative error of 1.73%. The skewness of the model in the test set toward the prediction results is 0.02, and the test results are approximated to the normal distribution. This further demonstrates that the current methodology enables promising robustness of the model.

Collectively, the prediction errors of this model are comparable to the continuous test measurement error requirements specified in the specification (JTG 3450-2019, 2019). Moreover, it has achieved stable performance on both the test and training sets.

In order to further estimate the performance of the model, this study also adopted the validity ratio to assess the predictive accuracy of the model. The above procedure is carried out immediately following the evaluation of model errors.

When the model iterated through the test set, each sample was predicted five times in succession. The prediction was considered valid if the difference between the maximum and minimum values is less than 3. The mathematical meaning of validity ratio is the percentage of valid samples to the total samples.

The RMSE values, variance, and validity ratio of the model under each replicate test are shown in Table 4.

The validity ratio serves for the comparison of the EffectiveTexture-Net with the BPT direct skid resistance test. Tentatively, the model performed (mean validity ratio of 98.57%) rather consistently in parallel trials and met the expectations of this study.

Table 5 showed the performance of the other prevailing networks assembled as the backbone of the EffectiveTexture-Net on the Effective Contact Texture Region dataset.

In real training tests, it can be found that the majority of the classical CNN architectures with pre-trained transfer learning have better performance. The deployment efficiency of the model can be improved by appropriate fine-tuning of the preprocessing and regression layers.

However, it is worth noting that deepening the network hierarchy overly cannot help much in terms of performance improvement. The residual leapfrog connectivity (i.e., ResNet) can significantly improve this issue. Furthermore, when ResNet-101 is serving as the backbone for transfer learning, the performance improvement, compared to the ResNet-50, is marginal, but the computational workload is significantly increased.

On the other hand, the transformer model with a self-attention mechanism, such as Swin Transformer (Ze Liu et al., 2021), also becomes one of the new state-of-the-art models in the field of computer vision for upstream tasks. Thus, the Swin-L version of the Swin Transformer is considered to be a comparison in this study as the backbone network for feature extraction of the effective contact texture regions.

When Swin-L is serving as the backbone, the performance of the model is moderately improved (approx. 0.79% reduction in relative error) over ResNet-50 as the backbone on the dataset after texture disentanglement. But the cost is a burst in the computational effort of about 12% extra. Moreover, the performance of the model with Swin-L as the backbone on datasets without texture disentanglement directly corresponds to the performance of ResNet-50 on datasets with texture disentanglement. This supports the feasibility and justification of using ResNet-50 as the backbone for this study under the prerequisite of texture disentanglement.

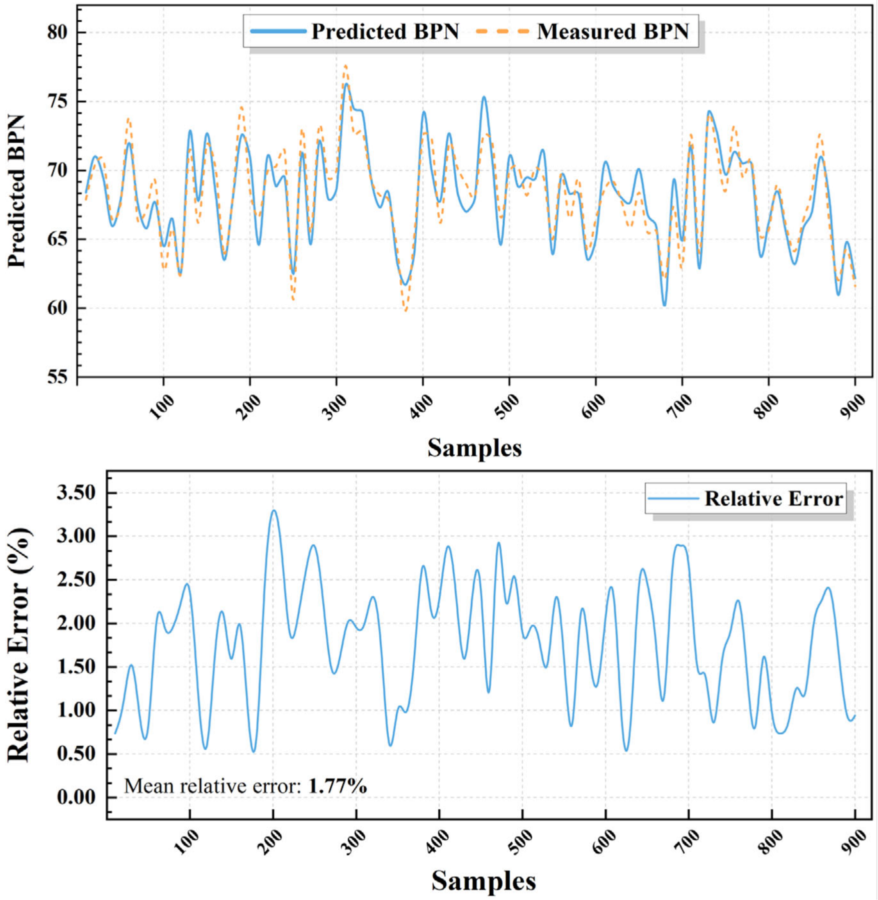

FIGURE 10 An example of one-trial predictive performance for the model. BPN, British pendulum number.

TABLE 4 Results of the repetitive tests.

	Performance of the model under each parallel isolated trial									
No.	**1st**	**2nd**	**3rd**	**4th**	**5th**	**6th**	**7th**	**8th**	**9th**	**10th**
RMSE value	1.362	1.347	1.337	1.326	1.343	1.358	1.378	1.287	1.411	1.436
S^2	0.724	0.687	0.818	0.792	0.837	0.596	0.739	0.821	0.855	0.764
Validity ratio	98.11%	98.78%	99.44%	98.22%	97.78%	98.33%	98.22%	98.67%	98.78%	99.44%

TABLE 5 Performance comparison of various models.

Model Name	AlexNet	VGG-11	VGG-16	VGG-19	ResNet-34	Swin-L	Effective Texture-Net
Training set absolute error	1.619	1.528	1.515	1.519	1.433	1.008	1.021
Test set absolute error	1.631	1.537	1.524	1.522	1.467	1.217	1.232
Test set relative error	3.82%	3.67%	3.27%	3.29%	2.07%	1.02%	1.81%

5.1.2 | Validation of effective contact texture region and texture disentanglement

To further validate the beneficial effect of the effective contact texture mechanism and texture disentanglement on the CNN model in this study, the ablation experiments were carried out under similar conditions in this section. Table 6 shows the variation of the model on the original texture, effective contact texture region dataset, and effective contact texture region dataset (with disentanglement).

The model based on the effective contact texture region showed a significant enhancement in the accuracy of prediction and evaluation (the relative error drops by 6.13%). In contrast, the results using the original texture region showed similar results to previous comparable studies, and considerable benefits were achieved by precisely matching

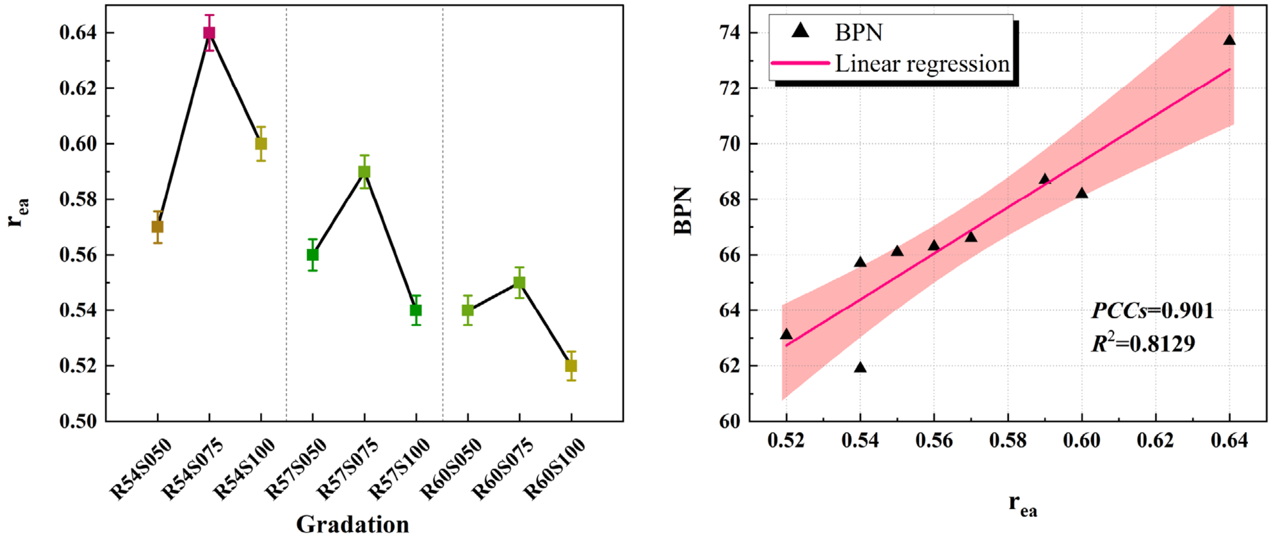

FIGURE 11 (a) The trend of the effective contact ratio of each gradation and (b) the linear relationship between the effective contact ratio and British pendulum number (BPN).

TABLE 6 The model performance on the original texture, effective contact texture region dataset, and effective contact texture region dataset (with disentanglement).

Dataset	Test set absolute error	Test set relative error
Original texture region	5.368	9.37%
Effective contact texture region (without disentanglement)	2.175	3.24%
Effective contact texture region (with disentanglement)	1.232	1.81%

the texture acquisition to test regions of the skid resistance one-to-one.

The expressivity of the model dataset is released further (the relative error reduced to 1.81%), when the macro-texture and micro-texture were disentangled with frequency domain analysis.

It is believed that this is due to the effective contact texture region proposed in this study, which filtered the raw textures favorably. This method retains valid information of high order and reduces the complexity of the dataset. It is a valuable way to study the possibility of reducing the volume of the network.

5.2 | Characteristics of the effective contact texture region

In this section, the point cloud after the maximum depth threshold segmentation process is utilized for triangulation, enabling easy gridding and easy access to the area of effective contact texture region.

As shown in Figure 11, it is easy to find that the area of effective contact texture region provided by varying gradation types of the asphalt mixture decreases relatively with the increase of coarse aggregate content. On the one hand, it indicates that the macro-texture does not significantly improve the richness of the local texture when the depth increases. On the other hand, the appropriate increase of the aggregate content from 2.36 to 4.75 mm particle size can rapidly improve the regional micro-texture content, which is a critical gain to increase the contact effect between the pavement texture area and vehicle tires. The more significant point is that the area of effective contact texture region for pavement texture is not a fixed value but varies within range and particularly exhibits a correlation with the relative proportions of macro-texture and micro-texture.

In the case of this study, the effective texture area reached a maximum of 54% coarse aggregate content and 7.5% aggregate content of 2.36 to 4.75 mm particle size, while the average effective contact ratio ranged from 0.52 to 0.64. There is a significant positive correlation between this parameter and the skid resistance of the pavement with a linear fitted Pearson correlation coefficient of 0.901 and an R^2 of 0.8129, which further indicates that the effective contact ratio parameter has the potential to be utilized in the experimental phase of asphalt mixtures for preliminary assessment of skid resistance.

6 | CONCLUSION

In contrast to the prevalent indirect feature prediction models based on texture parameters such as mean texture depth or MPD, this study proposed a CNN model based on 3D effective contact texture region to predict the skid resistance performance of pavements. This paper utilized BPT for the skid resistance test of asphalt mixture pavement, and a high-precision 3D laser scanner was used for the texture point clouds data acquisition.

The area characteristics of effective contact texture region for different types of asphalt mixtures were analyzed. Then the capability discrepancy of CNN models was visually investigated under other training methods. Finally, the performance of the model was validated. Based on this, the following conclusions can be drawn from this study:

1. Using the effective contact texture region that has been extracted by the maximum contact constraint decreases the redundancy of unnecessary information. Disentanglement of macro- and micro-scale textures based on the FFT for the above regions significantly improved the accuracy and precision of the EffectiveTexture-Net. The relative error of the EffectiveTexture-Net was ultimately 1.81%.
2. The contribution of the different backbone networks to the EffectiveTexture-Net varies considerably. Network structure being over-depth provides negligible benefits to model performance. Moreover, the network with residual leap-frog structure performs superiorly than the typical stacked network. When the backbone was ResNet-50, the model performed comparable to the Swin-L (Transformer), but with remarkably less computation.
3. The triangulation enables better fitting of orphan data in the effective texture point cloud after filtering by the maximum depth constraint. The dissection algorithm is easily implemented programmatically. It can further subdivide the grid to improve computational accuracy.
4. The surface area of the effective contact texture region can be efficiently obtained using triangulation, which is not a fixed value but varies dynamically depending on the key sieve passing rate from 2.36 to 4.75 mm of the mixture gradation. Meanwhile, the area exhibits a high correlation (*Pearson correlation coefficient* is 0.901, $R^2 = 0.8129$) with the skid resistance of the pavement.
5. The effective contact ratio obtained in this paper ranges from 0.52 to 0.64. The pavement skid resistance improves significantly with the increase of the effective contact ratio. This parameter is valuable for the design or preliminary evaluation of asphalt mixtures.

For further work, the influence of morphological properties of aggregates on the skid resistance of asphalt mixes will be considered and the new paradigm of neural networks will be merged with simulation modeling to establish more generalized evaluation metrics.

ORCID

Weibo Shi https://orcid.org/0000-0003-0140-7315
Dongyu Niu https://orcid.org/0000-0002-1736-5378

REFERENCES

Adeli, H. (2001). Neural networks in civil engineering: 1989–2000. *Computer-Aided Civil and Infrastructure Engineering*, *16*(2), 126–142.

Adeli, H. (2020). Four decades of computing in civil engineering. In C. Ha-Minh, D. Dao, F. Benboudjema ,S. Derrible, D. Huynh, A. Tang (Eds.), CIGOS 2019, innovation for sustainable infrastructure. lecture notes in civil engineering (pp. 3–11) Springer.

Ahammed, M. A, & Tighe, S. L. (2009). Early-life, long-term, and seasonal variations in skid resistance in flexible and rigid pavements. *Transportation Research Record: Journal of the Transportation Research Board*, *2094*(1), 112–120.

Alam, K. M. D. R, Siddique, N., & Adeli, H. (2020). A dynamic ensemble learning algorithm for neural networks. *Neural Computing and Applications*, *32*(10), 8675–8690.

ASTM. (2015). *Standard practice for calculating pavement macrotexture mean profile depth*. ASTM E1845-15.

ASTM. (2018). *Standard test method for measuring paved surface frictional properties using the dynamic friction tester*. ASTM E303-93.

Bengio, Y., & Lecun, Y. (2007). Scaling learning algorithms towards AI. In L. Bottou, O. Chapelle, D. DeCoste, & J. Weston (Eds.), *Large-scale kernel machines* (pp. 1–41). MIT Press.

Celko, J., Kovac, M., & Kotek, P. (2016). Analysis of the pavement surface texture by 3D scanner. In L. Rafalski & A. Zofka (Eds.), *6th Transport research arena (TRA)* (pp. 2994–3003). Elsevier.

Chen, B., Zhang, X., Yu, J., & Wang, Y. (2017). Impact of contact stress distribution on skid resistance of asphalt pavements. *Construction and Building Materials*, *133*, 330–339.

Chen, J., & He, Y. (2022). A novel U-shaped encoder–decoder network with attention mechanism for detection and evaluation of road cracks at pixel level. *Computer-Aided Civil and Infrastructure Engineering*, *37*(13), 1721–1736.

Chrisochoides, N., & Sukup, F. (1999). Task parallel implementation of the Bowyer-Watson algorithm. *Cornell Theory Center*, Cornell University.

Chu, L., Cui, X., Zhang, K., Fwa, T. F., & Han, S. (2019). Directional skid resistance characteristics of road pavement: Implications for friction measurements by British pendulum tester and dynamic friction tester. *Transportation Research Record*, *2673*(10), 793–803.

Chu, L. J., & Fwa, T. F. (2019). A functional approach for determining skid resistance threshold state of porous pavement. *International Journal of Pavement Engineering*, *20*(4), 481–489.

Ding, S., Wang, K. C. P., Yang, E., & Zhan, Y. (2021). Influence of effective texture depth on pavement friction based on 3D texture area. *Construction and Building Materials*, *287*(5-6), 123002.

Dong, S., Han, S., Wu, C., Xu, O., & Kong, H. (2022). Asphalt pavement macrotexture reconstruction from monocular image based on deep convolutional neural network. *Computer-Aided Civil and Infrastructure Engineering*, *37*(13), 1754–1768.

Duchi, J., Hazan, E., & Singer, Y. (2011). Adaptive subgradient methods for online learning and stochastic optimization. *Journal of Machine Learning Research*, *12*(7), 257–269.

ES-AENOR. (2020). *ISO 13473-1: Characterization of pavement texture by utilize of surface profiles - Part 1: Determination of mean profile depth*. UNE-EN ISO 13473-1-2020.

Grande, Z., Castillo, E., Mora, E., & Lo, H. K. (2017). Highway and road probabilistic safety assessment based on Bayesian network models. *Computer-Aided Civil and Infrastructure Engineering*, *32*(5), 379–396.

Han, S., Liu, M., & Fwa, T. F. (2018). Testing for low-speed skid resistance of road pavements. *Road Materials and Pavement Design*, *21*(5), 1312–1325.

Han, S., Sun, P., & Fwa, T. F. (2019). Relationships between internal structure and surface texture of asphalt mixtures. *Road Materials and Pavement Design*, *22*(4), 894–909.

He, K. M., Zhang, X. Y, Ren, S. Q., & S, J. (2016). Deep residual learning for image recognition. *2016 IEEE Conference on Computer Vision and Pattern Recognition (CVPR)*, Las Vegas, NV, USA (pp. 770–778).

JTG 3450–2019. (2019). Highway road base pavement field test protocols: JTG 3450–2019. Ministry of Transportation and Communications, Highway Research Institute of Ministry of Transportation.

Hofko, B., Kugler, H., Chankov, G., & Spielhofer, R. (2019). A laboratory procedure for predicting skid and polishing resistance of road surfaces. *International Journal of Pavement Engineering*, *20*(4), 439–447.

Ioffe, S., & Szegedy, C. (2015). Batch normalization: Accelerating deep network training by reducing internal covariate shift. *International Conference on Machine Learning*. Lille, France (pp. 448–456).

Jeong, J. H., Jo, H., & Ditzler, G. (2020). Convolutional neural networks for pavement roughness assessment using calibration-free vehicle dynamics. *Computer-Aided Civil and Infrastructure Engineering*, *35*(11), 1209–1229.

Kingma, D. P., & Ba, J. (2014). Adam: A method for stochastic optimization. arXiv preprint arXiv:1412.6980v9.

Kogbara, R. B., Masad, E. A., Kassem, E., Scarpas, A. T., & Anupam, K. (2016). A state-of-the-art review of parameters influencing measurement and modeling of skid resistance of asphalt pavements. *Construction and Building Materials*, *114*, 602–617.

Kogbara, R. B., Masad, E. A., Woodward, D., & Millar, P. (2018). Relating surface texture parameters from close range photogrammetry to Grip-Tester pavement friction measurements. *Construction and Building Materials*, *166*, 227–240.

Kouchaki, S., Roshani, H., Prozzi, J. A., Garcia, N. Z., & Hernandez, J. B. (2018). Field investigation of relationship between pavement surface texture and friction. *Transportation Research Record*, *2672*(40), 395–407.

Kulakowski, B. T., Henry, J. J., & Lin, C. (1990). *A closed-loop calibration procedure for a British pendulum tester*. https://www.astm.org/stp23356s.html

Kumar, A., & Gupta, A. (2021). Review of factors controlling skid resistance at tire-pavement interface. *Advances in Civil Engineering*, *2021*, 2733054.

Liu, C., & Xu, B. (2022). A night pavement crack detection method based on image-to-image translation. *Computer-Aided Civil and Infrastructure Engineering*, *37*(13), 1737–1753.

Liu, Z., Mao, H., Wu, C. Y., Feichtenhofer, C., Darrell, T., & Xie, S., (2022). A ConvNet for the 2020s. *2022 IEEE/CVF Conference on Computer Vision and Pattern Recognition (CVPR)*. New Orleans, LA, USA (pp. 11966–11976).

Lu, J., Pan, B., Liu, Q., Sun, M., Liu, P., & Oeser, M. (2022). A novel noncontact method for the pavement skid resistance evaluation based on surface texture. *Tribology International*, *165*, 107311.

Najafi, S., Flintsch, G. W., & Khaleghian, S. (2016). Pavement friction management—Artificial neural network approach. *International Journal of Pavement Engineering*, *20*(2), 125–135.

Pascanu, R., Montufar, G., & Bengio, Y. (2013). On the number of response regions of deep feed forward networks with piece-wise linear activations. *Arthritis & Rheumatism*, *58*(6), 1823–1832.

Paszke, A., Gross, S., Massa, F., Lerer, A., Bradbury, J., Chanan, G., Killeen, T., Lin, Z. M., Gimelshein, N., Antiga, L., Desmaison, A., Kopf, A., Yang, E., DeVito, Z., Raison, M., Tejani, A., Chilamkurthy, S., Steiner, B., Fang, L., … Chintala, S. (2019). PyTorch: An imperative style, high-performance deep learning library. *33rd Conference on Neural Information Processing Systems (NeurIPS), Neural Information Processing Systems (NIPS)*, Vancouver, Canada.

Puzzo, L., Loprencipe, G., Tozzo, C., & D'andrea, A. (2017). Three-dimensional survey method of pavement texture using photographic equipment. *Measurement*, *111*, 146–157.

Li, Q. J., Zhan, Y., Yang, G., Wang, K. C. P., & Wang, C. (2017). Panel data analysis of surface skid resistance for various pavement preventive maintenance treatments using long term pavement performance (LTPP) data. *Canadian Journal of Civil Engineering*, *44*(5), 358–366.

Rafiei, M. H., & Adeli, H. (2017). A new neural dynamic classification algorithm. *IEEE Transactions on Neural Networks and Learning Systems*, *28*(12), 3074–3083.

Rebay, S. (1993). Efficient unstructured mesh generation by means of delaunay triangulation and Bowyer-Watson algorithm. *Journal of Computational Physics*, *106*(1), 125–138.

Ruder, S. (2016). An overview of gradient descent optimization algorithms. arXiv preprint arXiv: 1609.04747v2.

JTG E20-2019. (2019). Standard test methods of bitumen and bituminous mixtures for highway engineering: JTG E20-2019. Ministry of Transportation and Communications, Highway Research Institute of Ministry of Transportation.

Liu, Z., Lin, Y. T., Cao, Y., Hu, H., Wei, Y. X., Zhang, Z., Lin, S., & Guo, B. (2021). Swin Transformer: Hierarchical vision transformer using shifted windows. *2021 IEEE/CVF International Conference on Computer Vision (ICCV)*. Montreal, QC, Canada (pp. 9992–10002).

JTG F40-2004. (2005). Technical specifications for highway asphalt pavement construction: JTG F40-2004. Ministry of Transportation and Communications, Highway Research Institute of Ministry of Transportation.

Tong, Z., Gao, J., Sha, A., Hu, L., & Li, S. (2018). Convolutional neural network for asphalt pavement surface texture analysis. *Computer-Aided Civil and Infrastructure Engineering*, *33*(12), 1056–1072.

Vilaça, J. L., Fonseca, J C., Pinho, A. C. M., & Freitas, E. (2010). 3D surface profile equipment for the characterization of the pavement texture–TexScan. *Mechatronics*, *20*(6), 674–685.

Wang, Y., Yang, Z., Liu, Y., & Sun, L. (2018). The characterisation of three-dimensional texture morphology of pavement for describing pavement sliding resistance. *Road Materials and Pavement Design*, *20*(5), 1076–1095.

Wasilewska, M., Gardziejczyk, W., & Gierasimiuk, P. (2020). Comparison of measurement methods utilized for evaluation the skid resistance of road pavements in Poland—Case study. *International Journal of Pavement Engineering*, *21*(13), 1662–1668.

Wesolowski, M., Zokowski, M., & Blacha, K. (2018). Investigations of pavement surface on airfields using laser scanning and measurement acoustic emission. *14th International Conference Mechatronic Systems and Materials (MSM)*, Zakopane, Poland.

WHO. (2018). Global status report on road safety 2018: Summary. *World Health Organization*.

Yan, Y., Ran, M., Sandberg, U., Zhou, X., & Xiao, S. (2020). Spectral techniques applied to evaluate pavement friction and surface texture. *Coatings*, *10*(4), 424.

Yang, G., Li, Q. J., Zhan, Y., Fei, Y., & Zhang, A. (2018). Convolutional neural network-based friction model using pavement texture data. *Journal of Computing in Civil Engineering*, *32*(6), 04018052.

Yang, G., Wang, K. C. P., & Li, J. Q. (2021). Multiresolution analysis of three-dimensional (3D) surface texture for asphalt pavement friction estimation. *International Journal of Pavement Engineering*, *22*(14), 1882–1891.

Yang, G., Yu, W., Li, Q. J., Wang, K., Peng, Y., & Zhang, A. (2021). Random forest-based pavement surface friction prediction using high-resolution 3D image data. *Journal of Testing and Evaluation*, *49*(2), 1141–1152.

Żarski, M., Wójcik, B., Książek, K., & Miszczak, J. A. (2022). Finicky Transfer Learning—A method of pruning convolutional neural networks for cracks classification on edge devices. *Computer-Aided Civil and Infrastructure Engineering*, *37*(4), 500–515.

Zhan, Y., Li, J. Q., Yang, G., Wang, K. C. P., & Yu, W. (2020). Friction-ResNets: Deep residual network architecture for pavement skid resistance evaluation. *Journal of Transportation Engineering Part B-Pavements*, *146*(3), 04020027.

Zhan, Y., Liu, C., Deng, Q., Feng, Q., Qiu, Y., Zhang, A., & He, X. (2022). Integrated FFT and XGBoost framework to predict pavement skid resistance using automatic 3D texture measurement. *Measurement*, *188*, 110638.

Zhang, H. Y., Chen, X. H., Xu, G., Huang, D., & He, J. C. (2019). Effect of surface texture variation on skid resistance of asphalt pavement. *19th COTA International Conference of Transportation Professionals (CICTP)—Transportation in China 2025*. Nanjing, China (pp. 987–998).

How to cite this article: Shi, W., Niu, D., Li, Z., & Niu, Y. (2023). Effective contact texture region aware pavement skid resistance prediction via convolutional neural network. *Computer-Aided Civil and Infrastructure Engineering*, 1–17. https://doi.org/10.1111/mice.13063